The Astrophysical Journal, 926:180 (19pp), 2022 February 20 https://doi.org/10.3847/1538-4357/ac4710

Emission-line Variability during a Nonthermal Outburst in the Gamma-Ray Bright Quasar 1156+295

Melissa K. Hallum[1], Svetlana G. Jorstad[1,2], Valeri M. Larionov[2,3,10], Alan P. Marscher[1], Manasvita Joshi[1,4], Zachary R. Weaver[1], Karen E. Williamson[1], Iván Agudo[5], George A. Borman[6], Carolina Casadio[7,8], Antonio Fuentes[5], Tatiana S. Grishina[2], Evgenia N. Kopatskaya[2], Elena G. Larionova[2], Liyudmila V. Larionova[2], Daria A. Morozova[2], Anna A. Nikiforova[2], Sergey S. Savchenko[2,3,9], Ivan S. Troitsky[2], Yulia V. Troitskaya[2], and Andrey A. Vasilyev[2]
[1] Institute for Astrophysical Research, Boston University, 725 Commonwealth Avenue, Boston, MA 02215, USA; mhallum@bu.edu, jorstad@bu.edu, marscher@bu.edu, m.joshi@northeastern.edu, zweaver@bu.edu, kwilliam@bu.edu
[2] Sobolev Astronomical Institute, St. Petersburg State University, St. Petersburg, Russia; t.s.grishina@spbu.ru, enik1346@rambler.ru, sung2v@mail.ru, lliudmila@yandex.ru, d.morozova@spbu.ru, a.a.nikiforova@spbu.ru, s.s.savchenko@spbu.ru, i.troitsky@spbu.ru, y.troitskaya@spbu.ru, andrey.vasilyev@spbu.ru
[3] Pulkovo Observatory, St.-Petersburg, 196140, Russia
[4] Research Computing, Information Technology Services, Northeastern University, USA
[5] Instituto de Astrofísica de Andalucía, CSIC, Apartado 3004, E-18080 Granada, Spain; iagudo@iaa.es, afuentes@iaa.es
[6] Crimean Astrophysical Observatory RAS, P/O Nauchny, 298409, Russia; borman.ga@gmail.com
[7] Foundation for Research and Technology, Hellas, IESL and Institute of Astrophysics, Voutes, 7110 Heraklion, Greece; ccasadio@ia.forth.gr
[8] Department of Physics, University of Crete, 71003, Heraklion, Greece
[9] Special Astrophysical Observatory, Russian Academy of Sciences, 369167, Nizhnii Arkhyz, Russia
Received 2021 January 27; revised 2021 December 17; accepted 2021 December 25; published 2022 February 23

Abstract

We present multi-epoch optical spectra of the γ-ray bright blazar 1156+295 (4C +29.45, Ton 599) obtained with the 4.3 m Lowell Discovery Telescope. During a multiwavelength outburst in late 2017, when the γ-ray flux increased to 2.5×10^{-6} phot cm^{-2} s^{-1} and the quasar was first detected at energies $\geqslant$100 GeV, the flux of the Mg II λ2798 emission line changed, as did that of the Fe emission complex at shorter wavelengths. These emission-line fluxes increased along with the highly polarized optical continuum flux, which is presumably synchrotron radiation from the relativistic jet, with a relative time delay of $\lesssim$2 weeks. This implies that the line-emitting clouds lie near the jet, which points almost directly toward the line of sight. The emission-line radiation from such clouds, which are located outside the canonical accretion-disk related broad-line region, may be a primary source of seed photons that are up-scattered to γ-ray energies by relativistic electrons in the jet.

Unified Astronomy Thesaurus concepts: High energy astrophysics (739); Blazars (164); Gamma-rays (637); Quasars (1319); High-luminosity active galactic nuclei (2034)

Supporting material: data behind figure

1. Introduction

Active galactic nuclei (AGNs) constitute the most luminous class of objects in the universe. They are also quite diverse, consisting of several different subclassifications that depend, in part, on the angle of observation relative to the symmetry axis. The basic model of an AGN includes a central supermassive black hole (SMBH), an accretion disk (AD) around the SMBH, a dusty torus (DT) in the equatorial plane, a multitude of ionized clouds emitting spectral lines (broad and narrow emission-line regions, BLR and NLR, respectively), and—in 5%–10% of the cases—an oppositely directed pair of relativistic plasma jets propelled out of the nucleus along the rotational axis of the AD (e.g., Urry & Padovani 1995). When an AGN with relativistic jets is oriented such that one of the jet axes lies within $\sim$10° of the line of sight, the object is classified as a blazar.

Blazars dominate the γ-ray sky outside the Galactic plane. Inverse Compton (IC) scattering of UV, optical, and near-infrared photons by relativistic electrons in the jet can produce the γ-rays (e.g., Sikora et al. 2009), although processes involving hadrons are also possible (e.g., Böttcher et al. 2013). A major question for the IC process is the source of the seed photons that are up-scattered. They could be synchrotron photons emitted by the jet (synchrotron self-Compton, or SSC, process; e.g., Bloom & Marscher 1996), or photons emitted from sources outside the jet (external Compton, or EC, mechanisms): the AD (Dermer & Schlickeiser 1994), BLR (Sikora et al. 1994), and/or DT (Błażejowski et al. 2000; Sokolov & Marscher 2005). The SSC integrated flux should not greatly exceed the IR-optical synchrotron flux from the same population of electrons, as is common during outbursts in quasars (Sikora et al. 2009).

The relative timing of flares in γ-ray light curves, and the appearance of superluminal knots in millimeter-wavelength Very Long Baseline Array (VLBA) images, suggest that the variable γ-ray emission occurs parsecs from the SMBH (Jorstad & Marscher 2016). This is supported by detections of very high-energy (VHE, $\geqslant$100 GeV) γ-rays in some quasars, since such photons cannot escape from subparsec regions owing to high pair-production opacities encountered as they propagate through the dense field of lower-energy photons (Aleksić et al. 2011). On the other hand, γ-ray production by the EC mechanism on parsec scales is problematic, since the density of seed photons from the sources listed above should be lower than needed to explain the observed γ-ray luminosities.

[10] Deceased.

The zero time delay between flares in the optical and γ-ray light curves observed in a number of blazars (e.g., Jorstad et al. 2013; Larionov et al. 2017; Weaver et al. 2019) suggests that the γ-ray and optical synchrotron emission regions are co-spatial. Additionally, since the AD and main BLR are located within a parsec of the central SMBH, neither can be the main source of seed photons for IC γ-rays produced on scales of several parsecs or more. Another source of seed photons on such scales appears necessary.

Many solutions to this seed-photon problem have been proposed, with varying complexity. For example, Ackermann et al. (2014) concluded that the γ-rays in the quasar 4C+21.35 were produced via a combination of SSC and EC mechanisms along the jet 2–3 parsecs from the SMBH, with the EC seed photons originating from the DT. However, if the DT lies near the equatorial plane, as expected in a blazar, it is unlikely that it can provide a sufficient density of seed photons to the polar jet to explain the observed γ-ray fluxes (see Joshi et al. 2014). A more complex proposal is that the seed photons originate from within a slower outer layer of the jet (MacDonald et al. 2015). However, Nalewajko et al. (2014) found this to be insufficient to explain the observed γ-ray flux without overpredicting the X-ray emission. On the other hand, Isler et al. (2015) have argued that in some cases the jet may provide enough ionizing photons to the canonical BLR to produce γ-rays within a parsec of the black hole, although this would require a photon field too dense to avoid the effects of pair-production opacity (Aleksić et al. 2011).

A possible solution to the above conundrum is that the source of the seed photons is a population of emission-line clouds located near the jet, but farther than $\sim$1 pc from the black hole. León-Tavares et al. (2015) have suggested that such clouds could be entrained in an outflow surrounding the parsec-scale jet. On the other hand, Punsly (2013) and Larionov et al. (2020) have found a time-variable red wing in the Mg II λ2798 broad emission-line profile in the blazar 3C 279. An increase in the flux of this red wing during a γ-ray/optical outburst of 3C 279 in late 2016 led Larionov et al. (2020) to propose that the spectral feature is emitted by polar clouds that are falling toward, rather than away from, the central SMBH.

While some studies of such variability of emission lines in blazars have been carried out previously (e.g., León-Tavares et al. 2013; Punsly 2013; Isler et al. 2015; León-Tavares et al. 2015), more detailed investigations are required to explore the general and detailed characteristics of the phenomenon and its relation to γ-ray emission. As part of an effort to provide such studies, here we present and interpret observations of the optical spectrum and optical and γ-ray light curves of the quasar 1156+195 (4C +29.45), which has a redshift $z = 0.72469 \pm 0.00035$ (Hewett & Wild 2010) and luminosity distance $D_\ell \approx 4.5$ Gpc for a Hubble constant $H_0 \approx 70$ km s^{-1} Mpc^{-1} within the currently favored Lambda cold dark matter cosmology with $\Omega_{\rm matter} \approx 0.3$ and $\Omega_{\rm Lambda} \approx 0.7$.

1156+295 is extremely variable and highly polarized at optical and radio wavelengths (Wills et al. 1983, 1992; Fan et al. 2006; Hovatta et al. 2007; Savolainen & Kovalev 2008). It is a flat-spectrum radio quasar with a core-jet structure on milliarcsecond scales (McHardy et al. 1990). From the width of its Mg II emission-line and optical continuum flux, Keck (2019) derived a mass of $\sim 9 \times 10^8\, M_\odot$ for the central SMBH. The quasar was first detected as a γ-ray source in the second Energetic Gamma Ray Experiment Telescope (EGRET) Catalog (Thompson et al. 1995), and since 2008 has been monitored by the Large Area Telescope (LAT) of the Fermi Gamma Ray Space Telescope. The VLBA-BU-BLAZAR program (Jorstad & Marscher 2016) has monitored 1156+295 since 2007 with monthly imaging with the VLBA within a sample of 37 bright γ-ray blazars at 43 GHz. These observations, as well as VLBA monitoring at 15 GHz (Lister et al. 2016), have determined that bright knots in the jet can move with superluminal apparent speeds up to 25c. From the apparent motions and the timescale of the observed decline in flux of such knots, Jorstad et al. (2017) derived a Doppler factor $\delta = 12 \pm 3$, Lorentz factor $\Gamma = 10 \pm 3$, and jet viewing angle $\Theta_\circ \leqslant 2.^\circ 5$ using data from 2008–13. Based on contemporaneous γ-ray and optical light curves along with VLBA monitoring, Ramakrishnan et al. (2014) constrained the location of the $\sim$1 GeV γ-ray emission in 1156+295 to lie close to the parsec-scale millimeter-wave core at 43 GHz. In addition,1156+295 was detected for the first time at very highγ-ray energies (VHE, $\geqslant$100 GeV) in 2017 December by the Very Energetic Radiation Imaging Telescope Array System (VERITAS; Mukherjee 2017) and the Major Astronomical Atmospheric Gamma Imaging Cherenkov Telescopes (MAGIC; Mirzoyan 2017).

In this paper, we study variability of the Mg II λ2798 and blended Fe II emission lines with respect to the continuum optical and γ-ray flux of 1156+295 in an effort to determine the location and kinematics of the line-emitting clouds. In Section 2 we present our observations of 1156+295 along with γ-ray and optical light curves, while in Section 3 we describe the data analysis. We discuss the results in Section 4 and draw conclusions in Section 5.

2. Observations

2.1. Light Curves

We have obtained optical photometric and polarimetric measurements of 1156+295 in the R band from 2014 December 9 to 2019 June 3, and calculated its γ-ray light curve during the same period (and through 2019 September 6) using the photon and spacecraft data provided by the Fermi Science Support Center. The optical photometric and polarization data were obtained at multiple telescopes: (1) Lowell Observatory's 4.3 m Lowell Discovery Telescope (LDT; Happy Jack, AZ; formerly the Discovery Channel Telescope); (2) 1.8 m Perkins telescope (PTO; Flagstaff, AZ); (3) 70 cm AZT-8 (Crimean Astrophysical Observatory); (4) 40 cm LX-200 (St. Petersburg, Russia); (5) 2.3 m Bok and 1.54 m Kuiper telescopes of Steward Observatory (Tuscon, AZ)[11] (Smith et al. 2009); and (6) 2.2 m Calar Alto telescope (Andalucía, Spain).[12]

We have used differential aperture photometry to obtain photometric measurements with comparison stars 2, 3, and 4 from Raiteri et al. (1998), except for the Steward observatory data (see Smith 2016). We have obtained 599 measurements in the R band, with brightness ranging from $18.4^{\rm m}$ to $13.4^{\rm m}$. The average uncertainty of an individual measurement is $\leqslant 0.05^{\rm m}$. Conversion of R-band magnitude to flux density, F_R, was based on the calibration given in Mead et al. (1990). In order to separate optical activity states, we used the average flux density, $\langle F_R \rangle = 0.58$ mJy, and its standard deviation, $\sigma_R = 0.75$ mJy, reported in Williamson et al. (2014), where these values were calculated over $\sim$10 yr. We classify the flux state of the source as "quiescent" if $F_R \leqslant \langle F_R \rangle$, as

[11] Publicly available at http://james.as.arizona.edu/~psmith/Fermi/.
[12] MAPCAT program: https://www.iaa.csic.es/~iagudo/research/MAPCAT/.

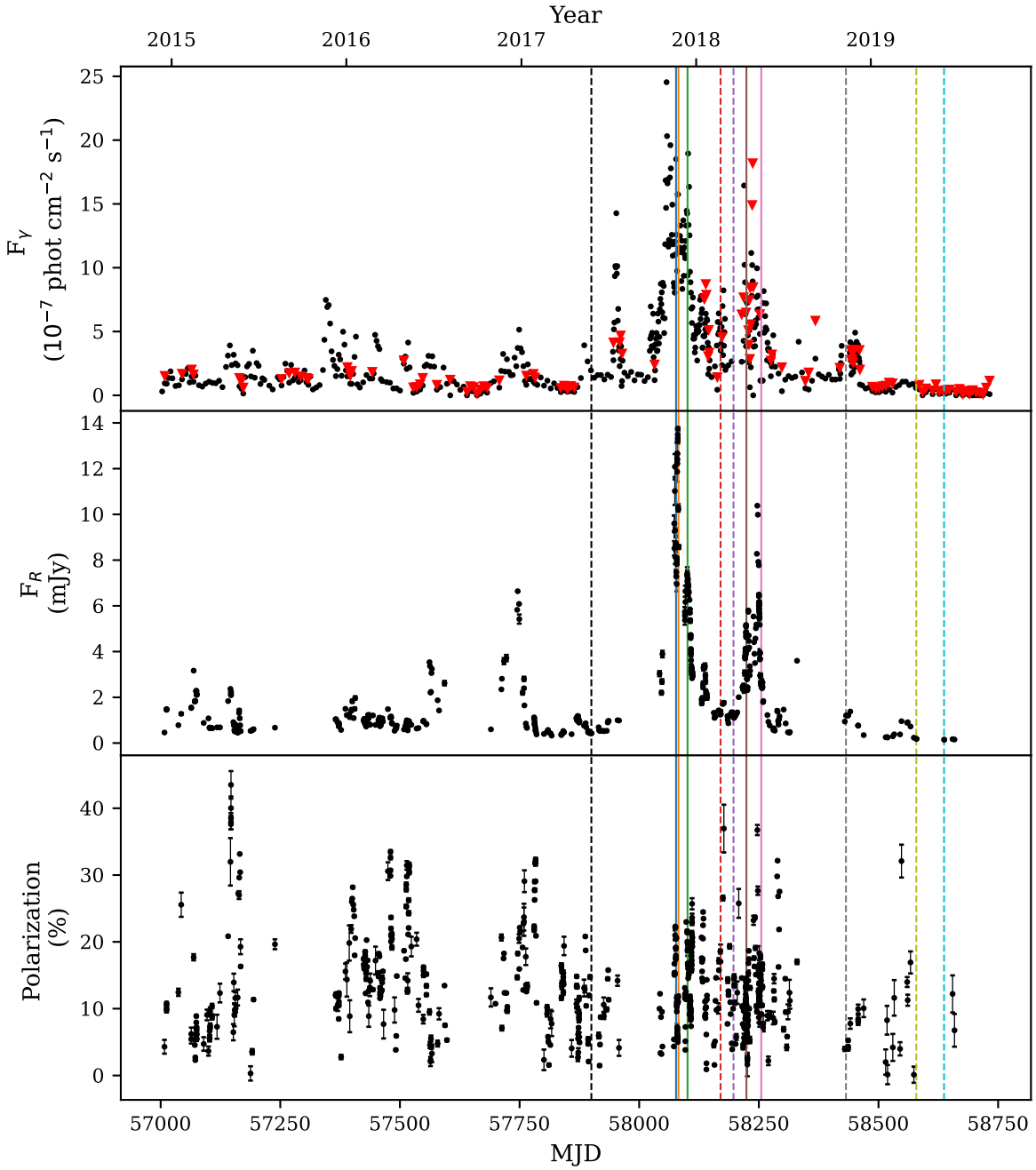

Figure 1. Gamma-ray and optical *R*-band light curves and polarization curve of 1156+295 from 2014 December to 2019 June. The colored vertical lines correspond to dates of our spectroscopic observations (see Figure 3), with the dashed lines indicating a quiescent or medium state, and the solid lines indicating an active state. The red downward triangles in the top panel represent upper limits. The uncertainty in the γ-ray flux depends on the brightness of the quasar and has an average value of 1.12×10^{-7} phot cm^{-2} s^{-1}.

"medium" if $\langle F_R \rangle < F_R \leqslant \langle F_R \rangle + 2\sigma_R$, and as "high" if $F_R > \langle F_R \rangle + 2\sigma_R$. This implies that a high state corresponds to $R < 15.4^{\rm m}$.

The polarization data were obtained in the *R* band at telescopes 2, 3, and 6 indicated above. The LX-200 telescope performed polarization measurements without a filter with central wavelength $\lambda_{\rm eff} \sim 6700$ Å. The Steward observatory telescopes used the Imaging/Spectro-polarimeter (Schmidt et al. 1992), which yields spectra in Stokes *q* and *u* parameters over a wavelength range from 4000 to 7500 Å (Smith 2016). These polarization parameters are close to *R*-band values. A brief discussion of data reduction for all telescopes can be found in Jorstad et al. (2010), who used the same telescopes and instruments to study the polarization behavior of the quasar 3C 454.3. The polarization parameters have been corrected for statistical bias (Wardle & Kronberg 1974).

We have reduced the γ-ray data using version v1.0.10 of the Fermi Science Tools, with background models from the iso_P8R3_SOURCE_V2_v1.txt isotropic template, and the gll_iem_v07 Galactic diffuse emission model.[13] We have employed an unbinned likelihood analysis of the photon data over an energy range of 0.1–200 GeV. The γ-ray emission of point sources within a 20° radius of the quasar was represented by spectral models listed in the fourth Fermi Large Area

[13] https://fermi.gsfc.nasa.gov/ssc/data/access/lat/BackgroundModels.html

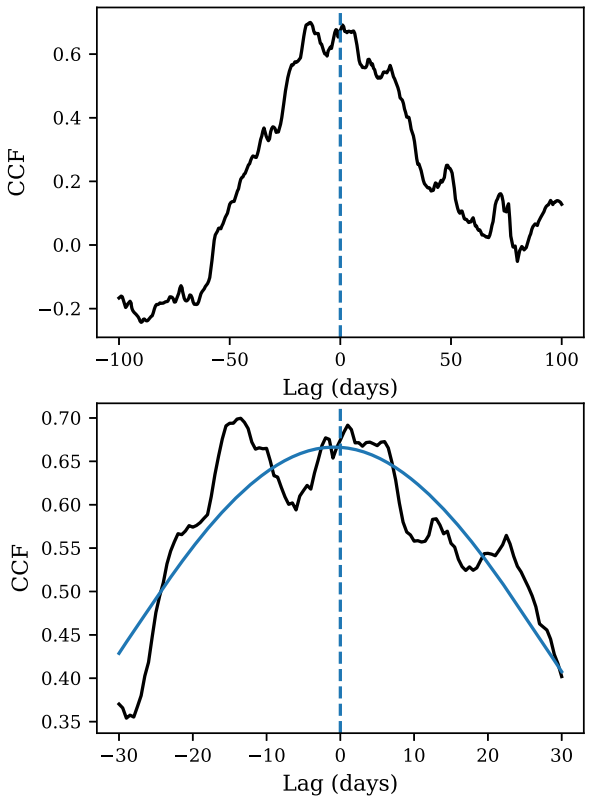

Figure 2. Top: cross-correlation function (CCF) between the optical and γ-ray light curves from 2016 April 22 to 2019 January 17; negative delay corresponds to the γ-ray light-curve leading. Bottom: best Gaussian fit to the peak of the CCF, centered on -0.81 ± 0.44 day, with FWHM 73 ± 2 day.

(The data used to create this figure are available.)

Telescope (4FGL) catalog of sources detected by the LAT (Abdollahi et al. 2020). The quasar's γ-ray spectrum was modeled by a log-parabola of the form

$$\frac{dN}{dE} = N_0 \left(\frac{E}{E_b}\right)^{-(\alpha+\beta \log E/E_b)}, \quad (1)$$

where $\alpha = 2.17$, $\beta = 6.75 \times 10^{-2}$, and break energy $E_b = 485$ MeV, as given in the 4FGL catalog. The spectral parameters of 1156+295 and all cataloged sources were kept fixed, with only the prefactor N_0 allowed to vary for 1156+295, catalog sources within 5°, and bright ($F_\gamma > 10^{-11}$ erg cm^{-2} s^{-1}) sources within 10°. We binned photons over 7 days during quiescent states as defined above based on optical observations, over 4 days during a medium state, and 1 day during an active state. The source was considered detected if the test statistic (produced in the maximum-likelihood analysis) $TS \geqslant 10$, which corresponds to a $\sim 3\sigma$ detection level (Nolan et al. 2012). If $TS < 10$, 2σ upper limits were calculated using the Python script provided by the Fermi Science Tools. The analysis resulted in 584 γ-ray measurements, out of which 127 are upper limits. During the high activity state in 2017 November–December, the γ-ray flux reached a value of $(2.7 \pm 0.2) \times 10^{-6}$ phot cm^{-2} s^{-1}, which corresponds to an apparent luminosity of $(4.7 \pm 0.4) \times 10^{48}$ erg s^{-1}.

The γ-ray and optical R-band light curves of 1156+295, along with the degree of polarization versus time, are displayed in Figure 1. As can be seen, the optical flare in late 2017 occurred at essentially the same time as a γ-ray flare. We have performed a cross-correlation analysis between the light curves using the PYCCF package (Peterson et al. 1998; Sun et al. 2018), which applies a linear interpolation between two unevenly sampled light curves. Setting the interpolation time step equal to 0.5 days, the analysis reveals a statistically significant correlation between the light curves, with a maximum correlation coefficient of 0.70 (see Figure 2). By fitting a Gaussian to the cross-correlation function (CCF) over lags of ±30 days, we determine that the γ-ray variations lead the optical variations by $\sim 0.8 \pm 0.5$ days in the observer frame (see Figure 2). The simultaneity of these flares within the uncertainties suggests that the emission sites of the two wave bands are co-spatial.

The fractional polarization of the quasar varied significantly during the outburst (from ∼1% to >30%), with an average value ∼15%. This implies that synchrotron emission dominated the optical continuum.

2.2. Spectral Observations

Optical spectroscopic and photometric observations of 1156+295 were carried out at the LDT. We observed the quasar 12 times between 2017 May 27 and 2019 June 3. The spectroscopic observations were performed using the DeVeny spectrograph,[14] with a grating of 300 grooves per millimeter and a slit width of 2.″5. This provided an observed wavelength range from about 3200 to 7500 Å, with a blaze wavelength of 5000 Å and a resulting dispersion of about 2.17 Å per pixel.

To measure the spectrum of 1156+295, we observed both the quasar and an A2 spectral-class comparison star, HD105199, which has a V-band magnitude of 9.83 and is located only 2.°17 from the quasar. An observation started with ∼2 exposures of the comparison star, followed by ∼3 exposures of 1156+295, and finished with ∼2 more exposures of HD105199. Additionally, we observed 1156+295 using the Large Monolithic Imager (LMI) at the LDT just before or after a spectral observation. We took ∼3 exposures in the R and V bands to provide photometry for the flux density calibration of the spectrum. A summary of these observations can be found in Table 1.

Each spectral image of the quasar and comparison star was checked for systematic errors, cleaned for cosmic rays, and corrected for bias and flat-field effects. The corrected spectra of HD105199, obtained before and after the quasar exposures, were summed. The same was done for the source spectra. This provided a signal-to-noise ratio for the 1156+295 and HD105199 spectra ⩾25 and >100, respectively.

We followed the technique of spectral reduction described in Vacca et al. (2003) and realized in an IDL program (v.8.6). Since HD105199 has a spectral class of A2, we have assumed that it has about the same intrinsic spectrum as Vega (A0). We performed shifting, scaling, and reddening of the Vega model spectrum (Castelli & Kurucz 1994) to match the summed spectrum of the comparison star. This allowed us to determine the point-spread function, atmospheric extinction, and position and profile of telluric lines during our observations, which were

[14] https://jumar.lowell.edu/confluence/pages/viewpage.action?pageId=23234141#DCTInstrumentationCurrent&Future-DeVeny

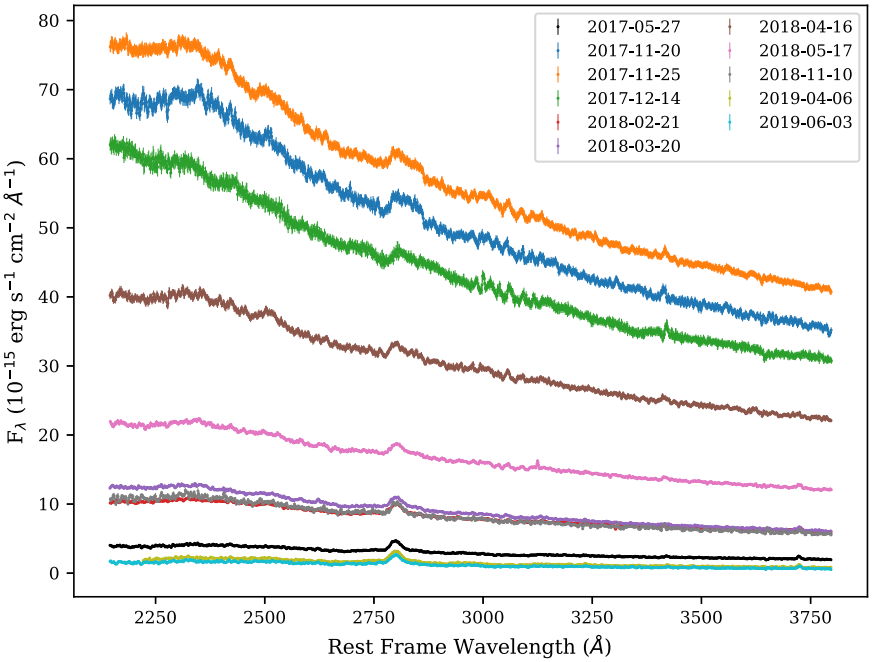

Figure 3. Optical spectra of 1156+295.

Table 1
LDT Observations of 1156+295

	DeVeny			LMI						
				V			*R*			
Date (yyyy-mm-dd)	MJD	*N*	Exp. (s)	*N*	Exp. (s)	mag	*N*	Exp. (s)	mag	State
(1)	(2)	(3)	(4)	(5)	(6)	(7)	(8)	(9)	(10)	(11)
2017-05-27	57900.24	2	1200	2	120	17.59 ± 0.01	2	90	17.19 ± 0.01	Q
2017-11-20	58077.49	3	600	0	⋯	⋯	3	30	14.08 ± 0.02	A
2017-11-25	58082.48	3	900	2	10	14.40 ± 0.01	2	10	13.93 ± 0.01	A
2017-12-14	58101.49	3	900	2	15	14.66 ± 0.01	2	10	14.23 ± 0.01	A
2017-12-24[a]	58111.40	3	900	0	⋯	⋯	3	60	15.10 ± 0.01	A
2018-02-21	58170.45	2	1200	2	30	16.47 ± 0.01	2	30	16.01 ± 0.01	M
2018-03-20	58197.45	2	900	2	15	16.40 ± 0.01	2	10	15.98 ± 0.01	M
2018-04-16	58224.15	5	750	2	15	15.07 ± 0.01	2	10	14.59 ± 0.01	A
2018-05-17	58255.26	3	1200	2	25	15.71 ± 0.01	2	15	15.25 ± 0.01	A
2018-11-10	58432.50	3	900, 600	2	60	16.50 ± 0.01	2	45	16.06 ± 0.01	M
2019-04-06	58579.30	3	1500	0	⋯	⋯	3	15	18.12 ± 0.01	Q
2019-06-03	58637.23	3	1500	3	40	18.60 ± 0.01	3	25	18.35 ± 0.01	Q

Note. Columns include: (1) The UT date of observations; (2) The UT of the DeVeny observations; (3, 5, 8) The number of exposures; (4, 6, 9) The exposure times in seconds; (7, 10) The measured magnitude of the quasar; (11) The state of the quasar during observations ("A" for active, "M" for medium, and "Q" for quiescent).
[a] Spectra from this date were excluded from the analysis due to bad weather conditions.

applied to calibrate the quasar's spectrum. We have estimated the uncertainty of the measured flux density in each spectrum by considering the following sources of error: (1) signal-to-noise ratio (S/N) of the data; (2) errors introduced during the reduction process; and (3) uncertainty in the wavelength dispersion. The S/N was determined by using the technique described in Stoehr et al. (2008). A total uncertainty in the flux of the emission lines of 2%–5% was then calculated as the sum of these uncertainties added in quadrature.

We have shifted the calibrated spectrum of the quasar into the rest frame using cosmological correction factors of $(1+z)^{-1}$ and $(1+z)^3$ for the wavelength λ and flux density F_λ, respectively. The resulting reduced spectra are displayed in Figure 3.

3. Spectral Analysis

The spectra presented in Figure 3 contain a prominent Mg II emission line at a rest-frame wavelength of 2798 Å, whose red wing rises as the continuum flux increases, as well as blended Fe II emission lines on both sides of Mg II, which also intensify with the continuum. To obtain parameters of the emission lines as a function of the continuum flux, we have modeled each spectrum as described below.

Table 2
Fe Windows

(1)	(2)	(3)	(4)	(5)
2250–2320	2333–2445	2470–2625	2675–2755	2855–3010

Note. All window ranges are in angstroms.

Table 3
Continuum Windows

(1)	(2)	(3)
2200–2230[a]	3030–3090[b]	3540–3600[b]

Notes. All window ranges are in angstroms.
[a] From Sameshima et al. (2011).
[b] From Tsuzuki et al. (2006).

3.1. Continuum Modeling

The optical continuum emission from a blazar-class quasar is often modeled as a combination of thermal radiation from an AD and synchrotron emission from a relativistic jet (e.g., Isler et al. 2015; Keck 2019). Since the synchrotron dominates over the thermal emission in 1156+295 (Ramakrishnan et al. 2014), as is the case for many blazars (e.g., Ghisellini et al. 2014; Larionov et al. 2020), the continuum can be modeled as a simple power law:

$$F_\lambda = F_\lambda(3000\ \text{Å})\left(\frac{\lambda}{3000\ \text{Å}}\right)^{\alpha}, \tag{2}$$

where $F_\lambda(3000\ \text{Å})$ is the flux density at the arbitrarily chosen reference wavelength of 3000 Å, and α is the spectral index. A possible complicating factor is the presence of the Balmer continuum (e.g., Grandi 1982; Kovačević et al. 2014). However, in the case of 1156+295, the synchrotron radiation is much brighter than the Balmer continuum radiation; therefore, we model the continuum as a simple power law.

AGNs often produce broad Fe-complex emission features, perhaps resulting from microturbulence in a confined gas (such as winds) or collisional excitation in warm, dense gas (Baldwin et al. 2004). Owing to the complexity of the electron energy levels of Fe, many Fe lines form at closely spaced wavelengths. These blend together to form broad pseudo-continuum emission features owing to a range of Doppler shifts from motions of the many clouds that emit the lines. The Fe emission must be taken into account when modeling the continuum and Mg II λ2798 spectral line. Therefore, we fit the power-law continuum model only in regions without significant Fe II or III emission.

Table 2 lists the Fe-complex windows present in our spectra, as identified by Vestergaard & Wilkes (2001), while Table 3 gives the continuum windows with little or no line emission, which we have used for fitting the continuum. Figure 4 plots the Fe and continuum windows for one of our spectra.

We carried out the power-law continuum fitting over each spectrum in the indicated continuum windows using the Levenberg-Marquardt least-squares method with the LMFIT python package (Newville et al. 2014). The fitted parameters are given in Table 4, and Figure 5 show the fits for all spectra.

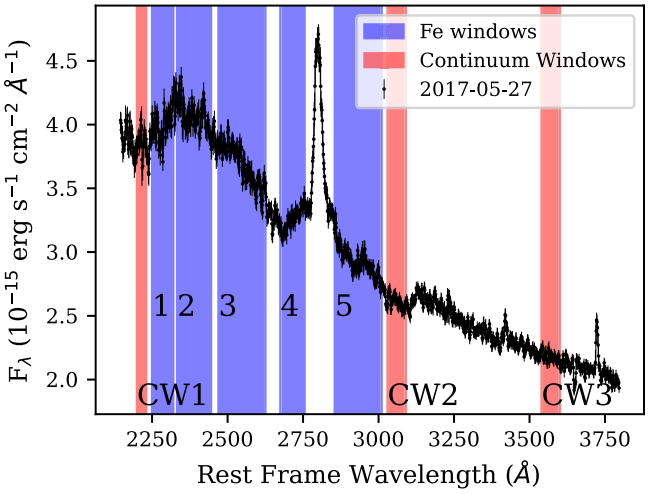

Figure 4. Spectrum of 1156+295 on 2017 May 27 with the Fe II/III complex and continuum windows.

Table 4
Continuum Fitting Results

Epoch yyyy-mm-dd (1)	S/N (2)	α_λ (3)	F $_\lambda$(3000) 10^{-15} erg s^{-1} cm^{-2}Å^{-1} (4)	$\chi^2_{\rm dof,Fe}$ (5)
2017-05-27	75	-1.207 ± 0.009	2.652 ± 0.004	0.689
2017-11-20	159	-1.220 ± 0.008	46.850 ± 0.065	1.269
2017-11-25	333	-1.148 ± 0.004	53.061 ± 0.042	0.606
2017-12-14	132	-1.259 ± 0.006	40.746 ± 0.040	0.552
2018-02-21	154	-0.985 ± 0.006	7.554 ± 0.008	0.713
2018-03-20	142	-1.320 ± 0.007	8.252 ± 0.011	1.014
2018-04-16	173	-1.068 ± 0.006	28.555 ± 0.028	0.735
2018-05-17	187	-1.048 ± 0.006	15.429 ± 0.017	0.902
2018-11-10	60	-1.197 ± 0.012	7.493 ± 0.015	0.936
2019-04-06	30	-1.590 ± 0.040	1.202 ± 0.006	1.245
2019-06-03	27	-1.517 ± 0.032	0.947 ± 0.005	1.387

Note. Columns are: (1) UT date of observation; (2) estimated S/N of the spectrum; (3) spectral index; (4) continuum flux density at 3000 Å; and (5) reduced χ^2 value for the Fe II template fit.

3.2. Mg II and Fe-complex Modeling

The Mg II λ2798 line is the most prominent emission line in our spectra. As can be seen in Figure 3, there appears to be a component redward of the core line centered at 2798 Å. This red wing appears to become brighter at higher flux states. We therefore model the Mg II λ2798 emission-line profile as the sum of two Gaussians (a "core" and "wing" component), each defined by:

$$f(\lambda; A, \mu, \sigma) = \frac{A}{\sigma\sqrt{2\pi}} \exp\left(-\frac{(\lambda-\mu)^2}{2\sigma^2}\right), \tag{3}$$

where A is the amplitude, μ is the central wavelength of the emission line, and σ is the standard deviation. The FWHM is then defined as:

$$\sigma_{\rm FWHM} = 2\sqrt{2\ln(2)}\,\sigma, \tag{4}$$

and is converted from wavelength space to velocity space using

$$\Delta v_{\rm FWHM} = c\frac{\sigma_{\rm FWHM}}{\mu}, \tag{5}$$

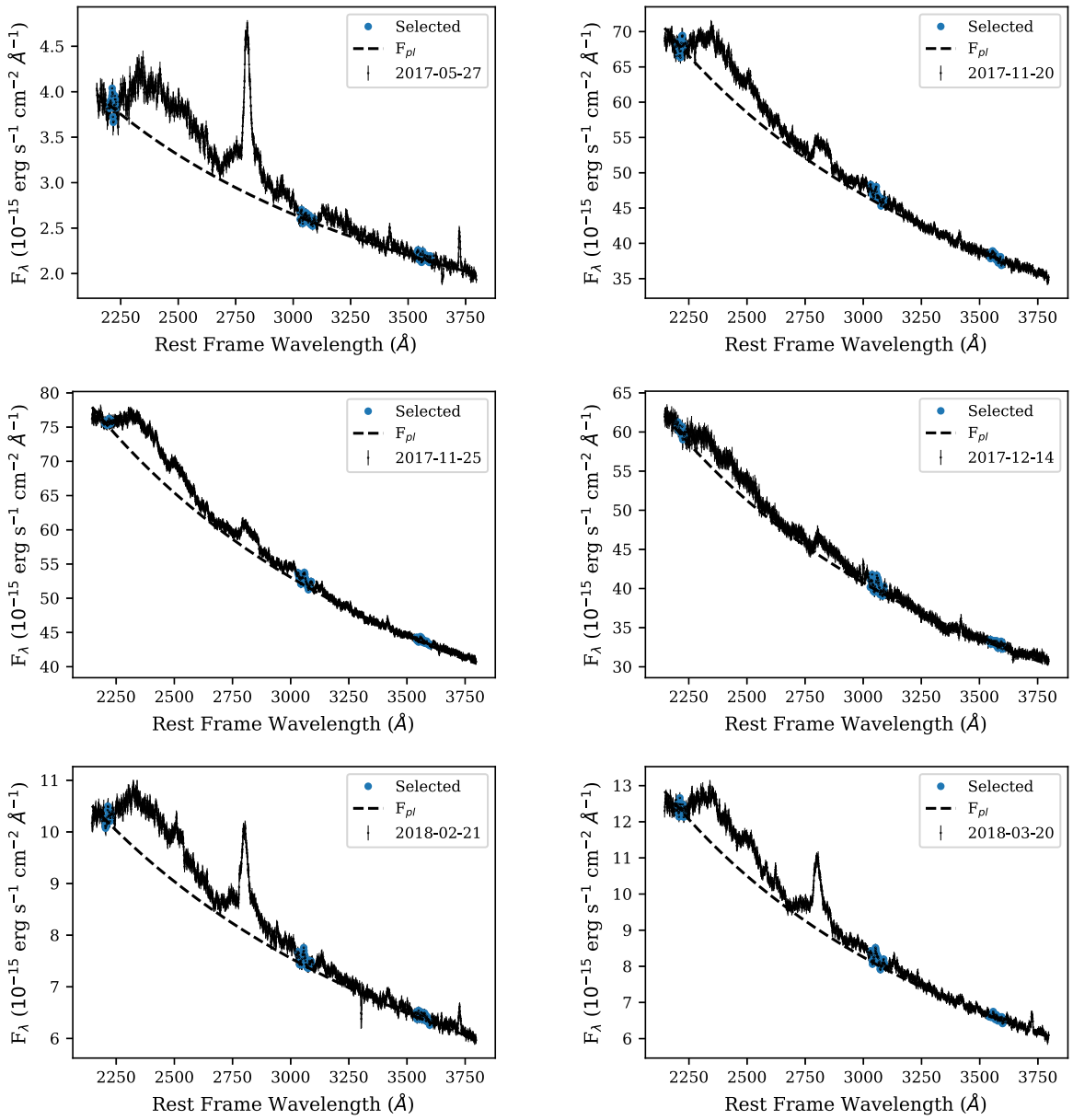

Figure 5. Spectra plotted with the best-fit continuum (dashed line).

where c is the speed of light.

As stated previously, our spectra consist of blended Fe II and III line complexes. Because these complexes extend to the region of the Mg II λ2798 emission line, it can be difficult to separate the Mg II lines from the Fe lines. To aid in doing so, we have utilized the Fe II and Fe III emission-line template composed by Vestergaard & Wilkes (2001). The Fe template was first convolved (in logarithmic wavelength space) with a Gaussian function that broadened the template lines to 3000 km s^{-1} (FWHM), as described by Vestergaard & Wilkes (2001). This FWHM was adopted because it is close to the average FWHM of our observed Mg II emission lines. (While in some cases one could attempt to determine the broadening using individual Fe lines in some regions of the spectra, e.g., Boroson & Green 1992, this is not possible for our observed spectra owing to the blended nature of the Fe lines in this region).

The IDL MPFIT fitting routine (which uses Levenberg-Marquardt least-squares minimization), as implemented by the python package hyperspy (de la Peña et al. 2021), was used to fit the double Gaussian profile and the broadened Fe template, with a scaling factor applied to each continuum-subtracted spectrum. We performed the fit in the 2650–2950 Å range of the rest-frame spectra. This region was chosen in order to include the Mg II emission line, as well as Fe windows 4 and 5 (as indicated in Table 2). We note that the Fe-complex template provided by Vestergaard & Wilkes (2001) contains multiple sub-templates. Of these, we use the UVA template and the UV47 template. The UV47 template is within the wavelength range of our spectra, but not within the range over which we perform our fitting routine. Because of this, we assume that UVA and UV47 have the same scaling factor. The parameters of the fit are reported in Table 5, and the fits are plotted in Figure 6. Additionally, we note that Table 5 reports the shift of

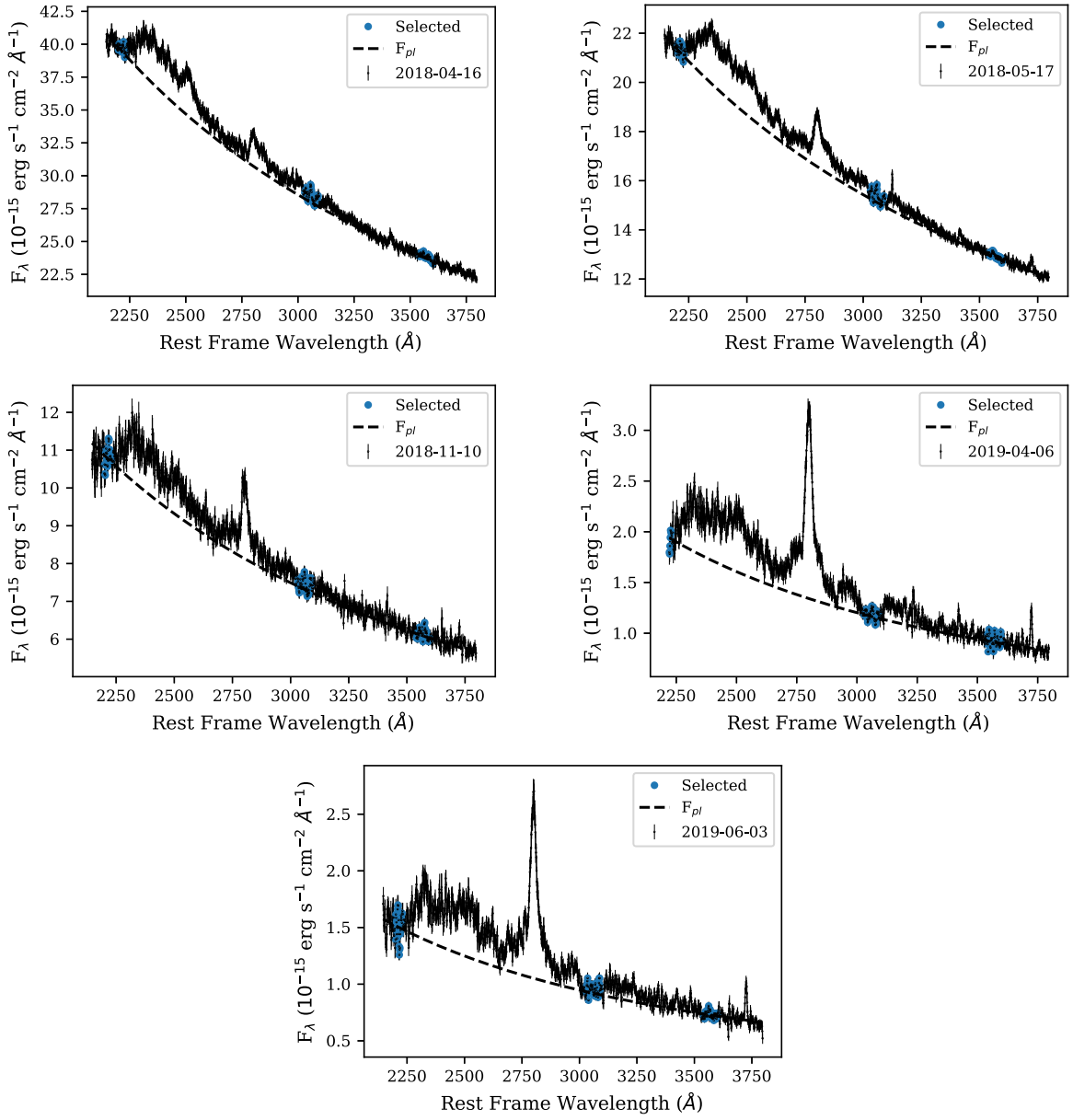

Figure 5. (Continued.)

Table 5
Results of Mg II λ2798 Emission-line Fitting

Epoch	Shift		FWHM		Flux		UVA	χ^2_{dof}
yyyy-mm-dd	km s^{-1}		km s^{-1}		10^{-15}erg s^{-1} cm^{-2}			
	Core	Wing	Core	Wing	Core	Wing		
(1)	(2)	(3)	(4)	(5)	(6)	(7)	(8)	(9)
2017-05-27	146 ± 30	5305 ± 238	3948 ± 62	1753 ± 582	67.2 ± 1.0	1.9 ± 0.6	0.051 ± 0.001	1.33
2017-11-20	1136 ± 93	5700 ± 147	4947 ± 247	1786 ± 354	185.1 ± 7.4	25.2 ± 5.4	0.232 ± 0.009	0.58
2017-11-25	736 ± 64	5787 ± 115	5035 ± 171	2104 ± 273	176.6 ± 4.9	26.4 ± 3.6	0.192 ± 0.006	0.27
2017-12-14	1237 ± 89	8933 ± 260	3817 ± 208	6954 ± 727	84.1 ± 4.4	71.5 ± 7.5	0.144 ± 0.007	0.26
2018-02-21	275 ± 31	5587 ± 269	4194 ± 77	2307 ± 660	79.3 ± 1.2	3.4 ± 0.9	0.067 ± 0.002	0.71
2018-03-20	392 ± 35	5645 ± 141	4445 ± 86	1980 ± 345	82.9 ± 1.3	5.6 ± 0.9	0.058 ± 0.002	0.65
2018-04-16	457 ± 66	5100 ± 226	4016 ± 170	2428 ± 540	98.1 ± 3.4	13.8 ± 3.1	0.146 ± 0.005	0.46
2018-05-17	456 ± 37	5885 ± 177	4252 ± 90	1438 ± 424	89.0 ± 1.6	3.6 ± 1.0	0.113 ± 0.002	0.44
2018-11-10	399 ± 52	6117 ± 133	3701 ± 119	668 ± 331	74.7 ± 2.1	1.9 ± 0.8	0.071 ± 0.003	0.90
2019-04-06	112 ± 34	5321 ± 270	4225 ± 75	1389 ± 661	72.7 ± 1.2	1.3 ± 0.6	0.047 ± 0.001	1.33
2019-06-03	96 ± 41	5012 ± 110	4327 ± 94	307 ± 237	61.5 ± 1.2	0.5 ± 0.3	0.041 ± 0.001	1.73

Note. Columns correspond to: (1) UT date of observation; (2–3) shift of the center of the Mg II measured line from 2798 Å rest wavelength for the core and wing component, respectively; (4–5) FWHM of the line profile for the core and wing component of Mg II, respectively; (6–7) flux of the core and wing components of Mg II line, respectively; (8) scale factor used for the Fe II/III template ; and (9) reduced χ^2 of the fit.

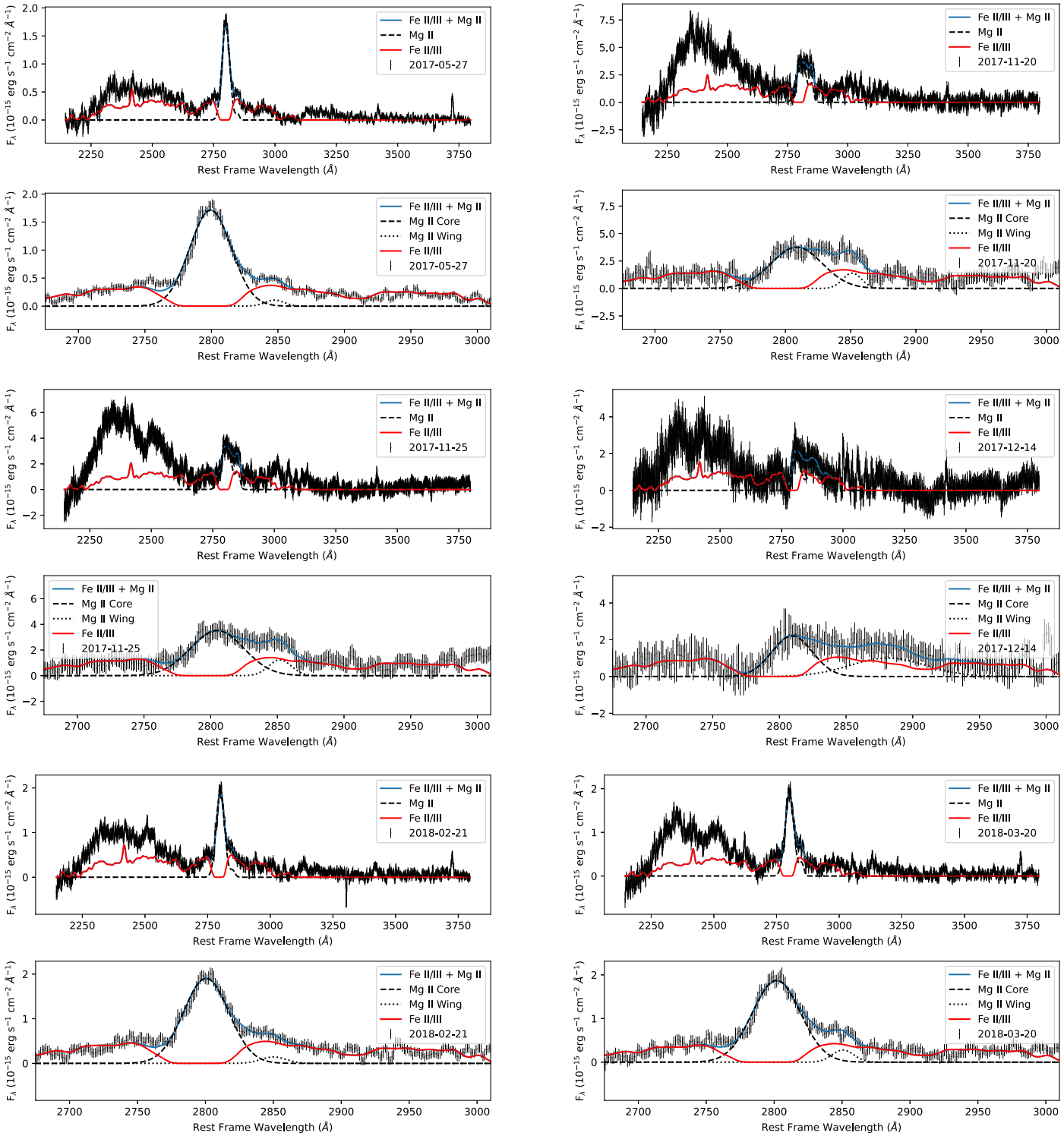

Figure 6. Continuum-subtracted spectra plotted with the best-fit Gaussian Mg II λ2798 emission-line profiles and scaled Fe II/III template (see the text).

the center of each of the fitted Gaussian components with respect to 2798 Å, a positive shift indicates that the Gaussian is centered redward of 2798 Å.

According to Table 5 the average shift of the central wavelength relative to that corresponding to the published redshift is only 123 ± 128 and 5095 ± 2932 km s^{-1} for the core and wing components, respectively, of the Mg II λ2798 emission line in the quiescent state, but 660 ± 208 and 6059 ± 1488 km s^{-1} in the active state. Thus, there appears to be no significant shift of the core component during quiescent states, but there may be a small shift redward during active states. Given the error ranges of the shifts of the wing component during active and quiescent states, it appears that the center of the wing does not change significantly from quiescent to active states, but remains several thousand kilometers per second redward of the line core. Table 5 also

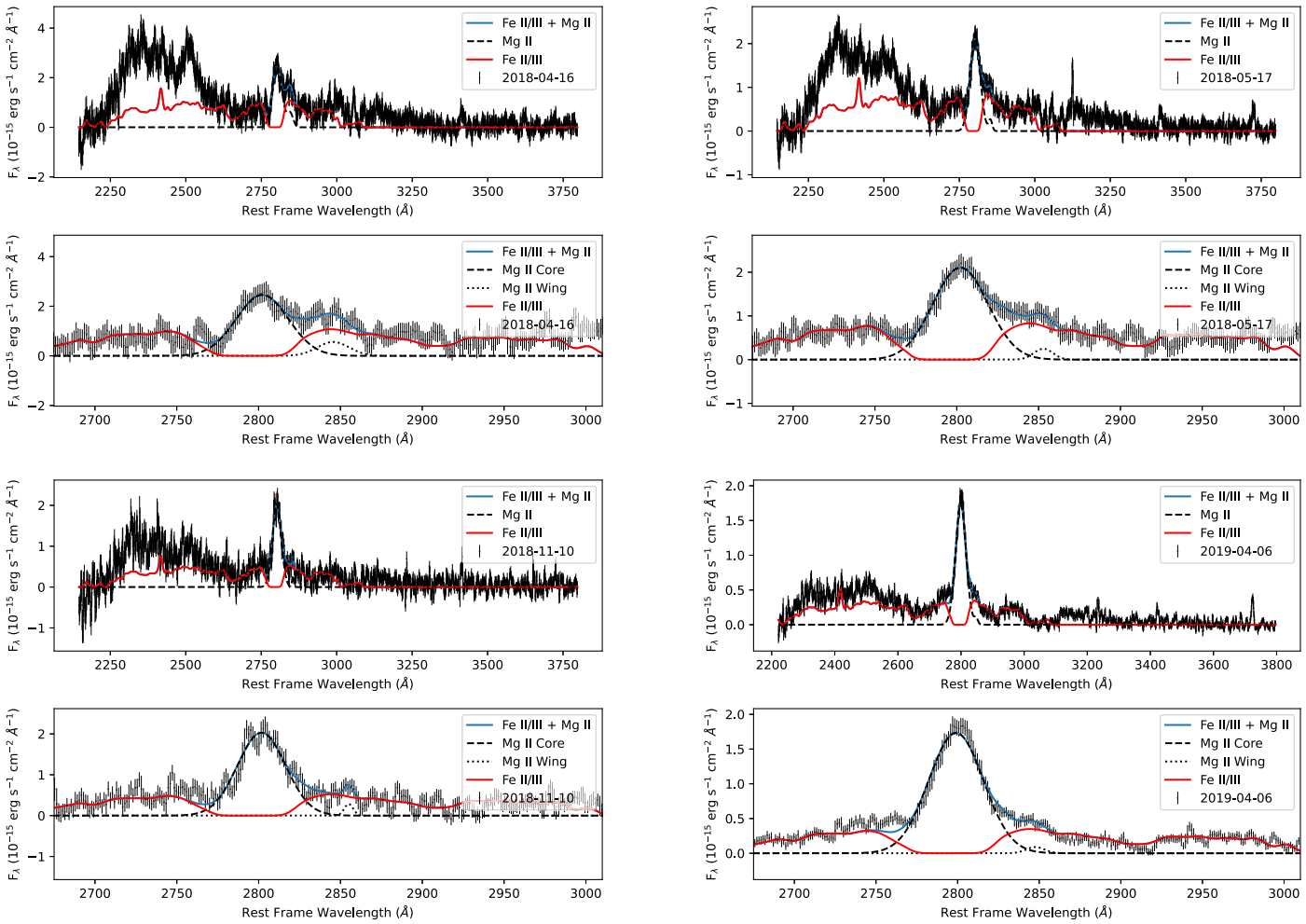

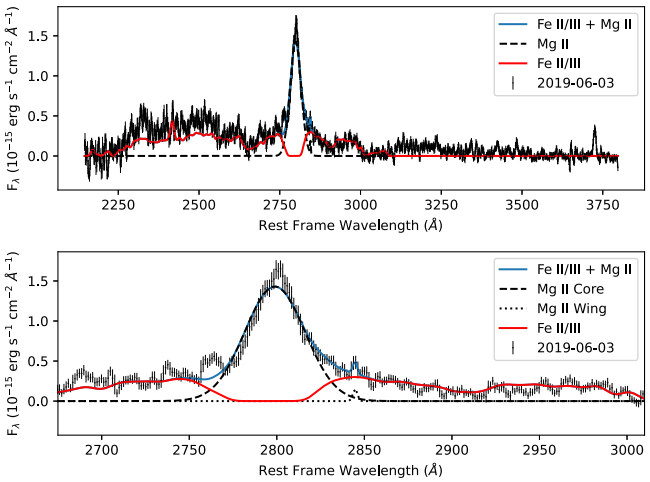

Figure 6. (Continued.)

shows that the red wing does generally increase in brightness during higher flux states.

As can be seen in Figure 6, the Fe template fits the emission well around the Mg II λ2798 line, but the template underestimates the Fe emission in the broad feature blueward of the Mg II line. This is discussed in greater detail in the following section.

3.3. Fe Emission

Figure 7 examines more closely the underestimation of the flux density of the broad emission feature blueward of the Mg II λ2798 line. The left panel of the figure presents each spectrum with just the continuum profile subtracted, while the right panel shows the same spectrum with the corresponding broadened and scaled Fe template subtracted as well. As can be seen in the

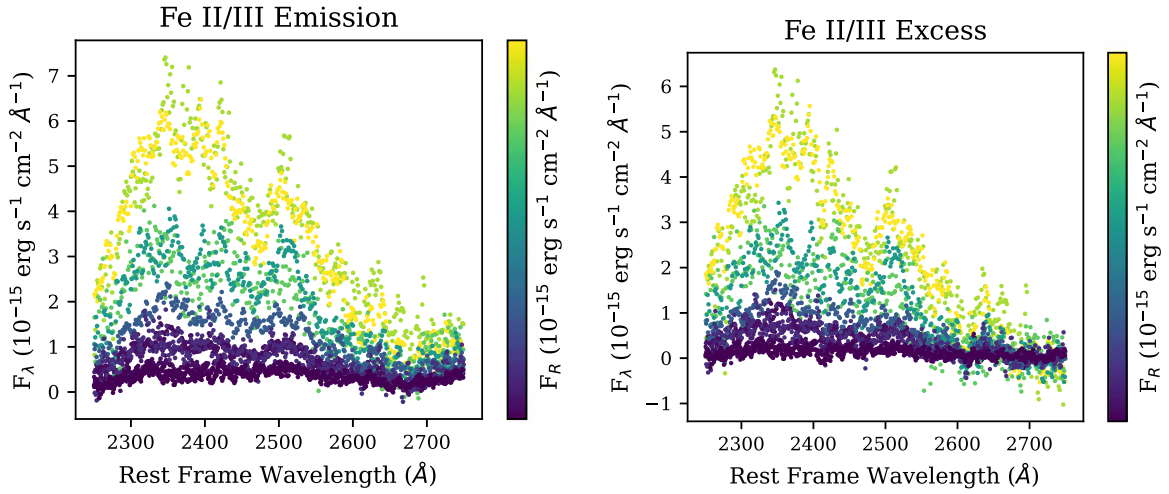

Figure 7. Left: the continuum-subtracted spectra in the 2250–2750 Å region. Right: the Fe II/III excess, i.e., difference between the continuum-subtracted spectra and the best-fit Fe templates. The color of each spectrum corresponds to the *R*-band magnitude of the source converted to flux density (see the color bar). (These spectra contain emission from non-Fe II/III lines as well; however, the Fe II/III lines dominate.)

Table 6
Fe II Emission Flux

Epoch yyyy-mm-dd (1)	$F_{\rm Fe,template}$ perg s^{-1} cm^{-2} (2)	$F_{\rm Fe,spec}$ perg s^{-1} cm^{-2} (3)
2017-05-27	126 ± 3	205 ± 2
2017-11-20	579 ± 23	1725 ± 21
2017-11-25	481 ± 15	1614 ± 19
2017-12-14	360 ± 18	906 ± 21
2018-02-21	168 ± 4	345 ± 3
2018-03-20	144 ± 5	361 ± 4
2018-04-16	365 ± 12	953±
2018-05-17	282 ± 6	602 ± 6
2018-11-10	178 ± 7	358 ± 7
2019-04-06	119 ± 3	183 ± 2
2019-06-03	102 ± 3	154 ± 2

Note. Columns include: (1) UT date of observation; (2) Fe flux from integrating the template spectrum; and (3) Fe flux from integrating the continuum and Mg II free spectrum over the wavelengths 2250–2750 Å. (It should be noted that these reported fluxes do contain emission from non-Fe II/III lines; however, the Fe II/III lines dominate.)

figure, the flux of the Fe emission complex increases with continuum flux, as does the residual after the fitted Fe template is subtracted. Table 6 reports the Fe emission flux as measured by integrating under the fitted template (Column 2), the flux as measured by integrating the continuum from 2250 to 2750 Å (Column 3), and the difference between these two values (Column 4). The Fe template is based on the Seyfert 1 galaxy I Zwicky 1, while the strength of the Fe-complex lines is known to vary across different objects (see Vestergaard & Wilkes 2001). The physical cause of this is poorly understood, and the general lack of knowledge about the main processes governing the strengths of the Fe lines leaves unexplained the discrepancy between the template and our spectra in the region blueward of the Mg II λ2798 emission line.

We have also performed the same fitting routine using an Fe II template by Popovic et al. (2018), finding that the general behavior of the Mg II λ2798 line, as well as the increase of the Fe II emission flux with the continuum, persist for this template as well. Additionally, the presence of a red-wing component of Mg II λ2798 is confirmed using this template. This wing also tends to be brighter when the blazar is in an active state. Details regarding the analysis using this Fe template can be found in the Appendix. In the discussion below we consider the results obtained with the template by Vestergaard & Wilkes (2001).

4. Discussion

The variations of the continuum, Mg II line, and Fe II/III complex fluxes are displayed in Figures 8 and 9. The maximum total luminosity of the Mg II plus Fe II/III lines is $\sim 7 \times 10^{45}$ erg s^{-1}, with the latter ∼9 times higher than the former. As can be seen in both figures, the Mg II and Fe II/III fluxes rise and fall with the continuum flux.

Although there are too few spectroscopic measurements to perform a robust correlation analysis, the near-simultaneity of the maximum observed line fluxes and maximum optical continuum flux strongly suggests a connection with a time delay $\lesssim$2 weeks. This implies that UV photons from the jet ionize the emission-line-producing clouds, which respond to variations in the jet flux with a short observed time delay, $\lesssim$2 weeks (see Figure 8). This can only be explained if the clouds producing the emission lines are located near the jet. We consider a cloud at a distance r from the source of the continuum flare in the jet and at a distance x from the jet axis. Changes in emission lines relative to continuum photons traveling directly along the line of sight from the flare site will occur with a light-travel time delay, Δt, governed by the expression

$$x \approx [c\Delta t'(c\Delta t' + 2r)]^{1/2}, \quad (6)$$

where $\Delta t' = \Delta t_{\rm obs}(1+z)^{-1}$ is measured in the rest frame of the host galaxy. This equation is valid for small viewing angles θ of the jet, such that $x \gg r\tan\theta$, as is the case for 1156+295 ($\theta \leqslant 2.^\circ 5$). For an observed time delay $\Delta t_{\rm obs} \sim 2$ weeks, $x \approx 0.1 r^{1/2}$ pc. This places the clouds in the environment immediately surrounding the parsec-scale jet.

The shift of the center of the Mg II line toward longer wavelengths during high flux states implies that the

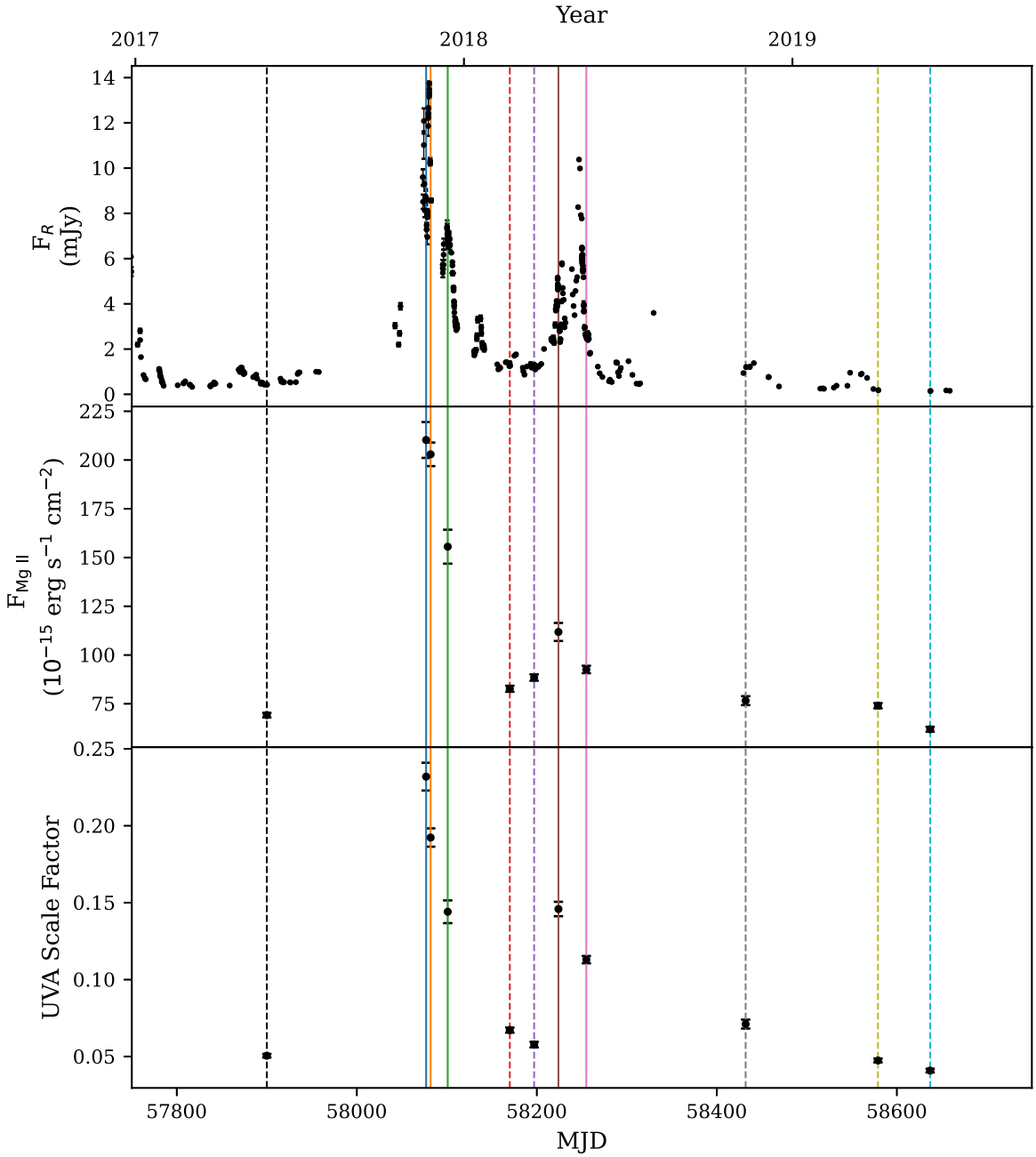

Figure 8. From top to bottom: optical continuum, Mg II emission-line, and Fe II/III emission-line fluxes of 1156+295 as a function of time. Vertical lines mark times of the spectroscopic observations.

contribution to the increase in line flux was greater for clouds receding more rapidly from us. This can be explained if the clouds are falling toward the SMBH. This is similar to, but not as large as, the shift seen in variations of the Mg II line in the blazar 3C 279. The latter included the appearance of a strong red wing to the line, centered $\sim$3500 km s^{-1} from the center of the pre-flare line (Punsly 2013; Larionov et al. 2020).

If the velocity shift were due to the freefall motion of the clouds in the gravitational potential of the SMBH, the distance from the SMBH of the clouds producing the red wing would be

$$R_{\rm ff} = 2R_g(c/v)^2. \quad (7)$$

Here, $R_g = GM/c^2$ is the gravitational radius, where G is the gravitational constant and M is the mass of the SMBH. The observed shift in the red wing is $\sim$5000 km s^{-1} for all spectra. The freefall distance of the red-wing clouds is therefore $\sim 7200R_g$. This is within the sphere of influence of the black hole (Zhou et al. 2019). The gravitational radius of the SMBH is 4.3×10^{-5} pc for our adopted mass of $9 \times 10^8 M_\odot$. The distance of the red-wing clouds would therefore need to lie within the inner 0.3 pc. However, the flare occurred simultaneously with a detection of VHE photons from the quasar, which cannot escape from a region so close to the SMBH, as discussed in Section 1. We therefore conclude that the excess redshift of these clouds is not caused by gravitational infall.

The origin and kinematics of the infalling polar clouds are thus challenging to explain. One possibility is that the clouds are entrained in a backflow from the interaction between the

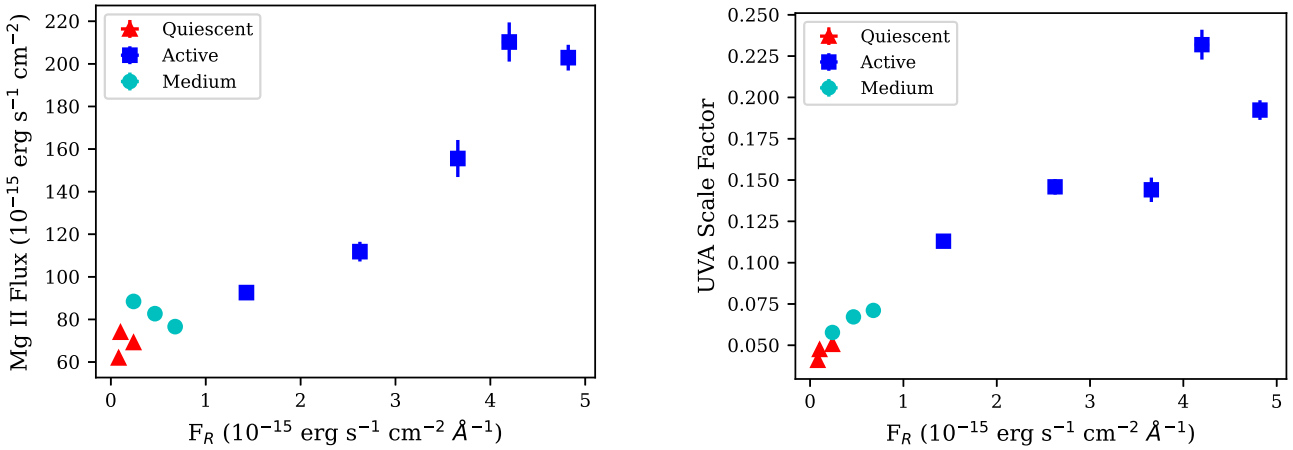

Figure 9. Emission-line fluxes of Mg II (left) and Fe II (right) versus the *R*-band flux density.

terminus of the jet and the kiloparsec-scale interstellar medium (which can flow toward the AD at a speed as high as ∼20,000 km s^{-1}; e.g., Norman & Miley 1984; Cielo et al. 2014; Perucho et al. 2019). Another proposal is that the clouds (as well as nonpolar emission-line gas) are condensations within an accretion-disk wind, dense regions that fail to reach the escape velocity, causing them to fall back toward the SMBH (Elvis 2017). Such polar clouds should be optically thin; otherwise, the line radiation along the line of sight—which lies within 2°.5 of the jet axis—would be shielded. However, the freefall velocity of the condensations at $r \sim 6$ pc would be much less than the observed values of ∼5000 km s^{-1} (see Table 5).

The symmetry of the observed emission lines in 1156+295 is difficult to reproduce with a model based on pure inflow. If all of the red-wing clouds were moving toward the SMBH, the Mg II line profile would be skewed toward the long or short wavelength side, depending on whether the radial velocity increases toward larger or smaller distances *r* from the SMBH. The velocities of the clouds could have a turbulent component that accounts for most of the line width. Such turbulence would be natural for clouds embedded in a backflow, caused by Kelvin–Helmholtz instabilities at the interface with the jet (Cielo et al. 2014; Perucho et al. 2019). The turbulence should be stronger closer to the jet, which could account for the increased breadth of the Mg II line during the outburst in 1156+295, to which clouds closest to the jet respond first.

The existence of broad-line-emitting clouds near the jet provides a possible source of seed photons for γ-ray production. (The observed ratio of maximum γ-ray to optical luminosity of ∼10 implies that EC rather than SSC scattering dominates the γ-ray production; see Section 1.) As discussed in Section 1, VHE emission produced in the subparsec region around the SMBH is suppressed due to pair production (Aleksić et al. 2011). The quasar was detected at energies $E > 100$ GeV on 2017 December 12 (Mirzoyan 2017), ∼2 weeks after we measured the maximum flux of the Mg II line and Fe II complex (see Tables 5 and 6). Note also that during these two weeks a significant increase in the degree of optical polarization, up to ∼22%, was observed (see Figure 1), confirming that the optical flare was nonthermal, and hence represents beamed emission from the jet. Therefore, if emission-line clouds near the axis of the jet are providing the seed photons, they must also be located beyond the inner parsec-sized region. If the clouds producing the variable emission lines are located at $r \sim 6$ pc, as in the wind condensation model discussed above, the energy density of the line photons at this distance is $\sim 5 \times 10^{-3}$ erg cm^{-3} in the rest frame of the jet. This is sufficient to provide the seed photons needed to explain a typical ∼1 GeV γ-ray flare (e.g., Joshi et al. 2014).

5. Conclusions

Based on our spectroscopic and continuum flux monitoring, we conclude that polar clouds, situated alongside the jet and located parsecs from the central SMBH, are ionized by UV photons from flares of synchrotron radiation originating farther upstream in the jet. This increases the flux of the Mg II λ2798 Å line and Fe II emission complex, with a time delay $\lesssim$2 weeks. We sketch the inferred location of this extended broad-line region in Figure 10.

The variations of the Mg II line are similar to, but less extreme than, those seen in 3C 279 (Punsly 2013; Larionov et al. 2020), with the line broadening and the central wavelength shifting to longer values when the continuum flux is higher. In order to sample the range of behavior of the emission lines in blazars, we plan to continue to follow changes in the emission lines of 1156+295, as well as those of other γ-ray flaring blazars.

We thank the referee for constructive comments that improved the paper. We are grateful to M. Vestergaard for providing the Fe emission template. This research was supported in part by NASA Fermi guest investigator program grants 80NSSC19K1504 and 80NSSC20K1565. We thank A. Tchekhovskoy for discussion of possible origins of the variable line-emitting clouds. These results made use of the Lowell Discovery Telescope (LDT) at Lowell Observatory. Lowell Observatory is a private, nonprofit institution dedicated to astrophysical research and public appreciation of astronomy, and operates the LDT in partnership with Boston University, the University of Maryland, the University of Toledo, Northern Arizona University and Yale University. This study was based in part on observations conducted using the 1.8 m Perkins Telescope Observatory (PTO) in Arizona, which is owned and operated by Boston University. I.A. acknowledges financial support from the Spanish "Ministerio de Ciencia e Innovación" (MCINN) through the "Center of Excellence

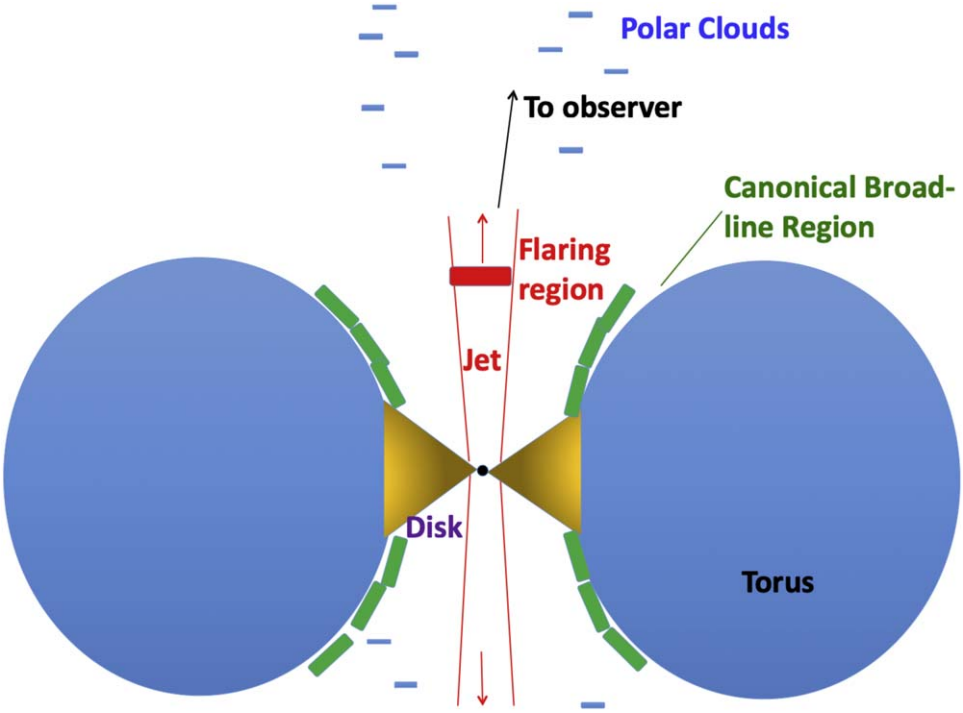

Figure 10. Sketch of the possible locations of the main components of the quasar 1156+295, which may represent that of blazars in general.

Severo Ochoa" award for the Instituto de Astrofísica de Andalucía-CSIC (SEV-2017-0709). Acquisition and reduction of the MAPCAT data were supported in part by MICINN through grants AYA2016-80889-P and PID2019-107847RB-C44. The MAPCAT observations were carried out at the German-Spanish Calar Alto Observatory, which is jointly operated by Junta de Andalucía and Consejo Superior de Investigaciones Científicas. Data from the Steward Observatory spectropolarimetric monitoring project were used; this program was supported by Fermi Guest Investigator grants NNX08AW56G, NNX09AU10G, NNX12 AO93G, and NNX15AU81G. C.C. acknowledges support from the European Research Council (ERC) under the European Union Horizon 2020 research and innovation program under the grant agreement No. 771282.

Facilities: LDT (DeVeny, LMI), Perkins, Fermi.

Software: Astropy, (The Astropy Collaboration et al. 2013, 2018), HyperSpy, (de la Peña et al. 2021) LMFIT (Newville et al. 2014) Matplotlib (Hunter 2007), NumPy (Harris et al. 2020), Specutils (Earl et al. 2020), uncertainties (Lebigot 2020), SciPy (SciPy 1.0 Contributors et al. 2020), SQLAlchemy Bayer (2012), pandas (Reback et al. 2020), PyCCF (Peterson et al. 1998; Sun et al. 2018).

Appendix

The Fe II template created by Popovic et al. (2018) is a composite of the Fe II multiplets 60, 61, 62, 63, and 78, as well as additional Fe II emission lines found in the quasar I Zw 1. The template covers the rest-frame wavelength range 2650–3050 Å. Each component is scaled arbitrarily relative to each other. We used the 3000 $\mathrm{km\,s^{-1}}$ FWHM broadened template and employed the same fitting procedures as we did when using the template from Vestergaard & Wilkes (2001). The fitted parameters are reported in Table 7, and are plotted in Figure 11. The fitted Mg II flux and Fe II flux versus the *R*-band flux density are plotted in Figure 12. The Mg II emission and the Fe II emission increase with the continuum as in the case of usage of the template by Vestergaard & Wilkes (2001; see Figure 9).

Table 7
Results of Mg II λ2798 Emission-line Fitting When Using the Fe II Template from Popovic et al. (2018)

Epoch	Shift		FWHM		Flux		Fe Template Scale						χ^2_{dof}
yyyy-mm-dd	km s^{-1}		km s^{-1}		10^{-15}erg s^{-1} cm^{-2}								
	Core	Wing	Core	Wing	Core	Wing	Mul. 60	Mul. 61	Mul. 62	Mul. 63	Mul. 78	IZw1lines	
(1)	(2)	(3)	(4)	(5)	(6)	(7)	(8)	(9)	(10)	(11)	(12)	(13)	(14)
2017-05-27	178 ± 35	⋯	3680 ± 77	⋯	64.1 ± 1.2	⋯	0.016 ± 0.001	0.015 ± 0.001	0.020 ± 0.003	0.000 ± 0.007	0.016 ± 0.002	0.017 ± 0.002	2.399
2017-11-20	880 ± 142	6401 ± 149	4406 ± 394	811 ± 365	164.6 ± 12.0	10.7 ± 4.5	0.059 ± 0.013	0.075 ± 0.011	0.064 ± 0.026	0.004 ± 0.060	0.149 ± 0.018	0.125 ± 0.013	1.538
2017-11-25	573 ± 119	6390 ± 147	4827 ± 367	1115 ± 356	167.7 ± 10.2	13.3 ± 4.2	0.049 ± 0.011	0.071 ± 0.009	0.022 ± 0.022	0.088 ± 0.053	0.128 ± 0.015	0.075 ± 0.015	1.083
2017-12-14	1182 ± 134	6665 ± 179	3591 ± 335	1082 ± 420	81.1 ± 6.3	9.0 ± 3.4	0.018 ± 0.012	0.012 ± 0.020	0.001 ± 0.016	0.129 ± 0.040	0.082 ± 0.012	0.053 ± 0.011	0.669
2018-02-21	308 ± 41	6747 ± 263	3972 ± 108	1536 ± 631	76.4 ± 1.7	2.6 ± 1.1	0.020 ± 0.002	0.023 ± 0.002	0.026 ± 0.001	0.000 ± 0.000	0.024 ± 0.003	0.019 ± 0.003	1.580
2018-03-20	390 ± 42	6321 ± 109	4146 ± 114	887 ± 257	78.7 ± 1.8	2.6 ± 0.7	0.015 ± 0.002	0.019 ± 0.002	0.021 ± 0.005	0.007 ± 0.011	0.032 ± 0.003	0.017 ± 0.003	1.286
2018-04-16	427 ± 87	6493 ± 157	3909 ± 229	622 ± 372	95.2 ± 4.6	3.2 ± 1.7	0.043 ± 0.007	0.059 ± 0.005	0.041 ± 0.013	0.003 ± 0.032	0.093 ± 0.010	0.066 ± 0.005	1.333
2018-05-17	443 ± 67	6444 ± 250	4122 ± 183	1254 ± 577	86.7 ± 3.1	3.8 ± 1.8	0.034 ± 0.004	0.038 ± 0.003	0.025 ± 0.008	0.035 ± 0.018	0.053 ± 0.006	0.037 ± 0.004	1.504
2018-11-10	449 ± 56	6171 ± 118	3598 ± 139	725 ± 294	73.2 ± 2.4	2.7 ± 1.0	0.014 ± 0.003	0.022 ± 0.003	0.025 ± 0.007	0.016 ± 0.015	0.039 ± 0.005	0.019 ± 0.003	1.230
2019-04-06	160 ± 38	⋯	3858 ± 87	⋯	69.1 ± 1.4	⋯	0.013 ± 0.001	0.011 ± 0.001	0.022 ± 0.003	0.002 ± 0.007	0.022 ± 0.002	0.016 ± 0.002	1.926
2019-06-03	138 ± 49	⋯	3954 ± 120	⋯	58.6 ± 1.5	⋯	0.010 ± 0.001	0.012 ± 0.001	0.015 ± 0.003	0.007 ± 0.007	0.019 ± 0.002	0.015 ± 0.002	2.452

Note. Columns correspond to: (1) UT date of observation; (2–3) shift of the center of the Mg II measured line from 2798 Å rest wavelength for the core and wing component, respectively; (4–5) FWHM of line profile for the core and wing component of Mg II, respectively; (6–7) flux of the core and wing components of Mg II line, respectively; (8–13) scale factors used for the Fe II template; and (14) reduced χ^2 of the fit.

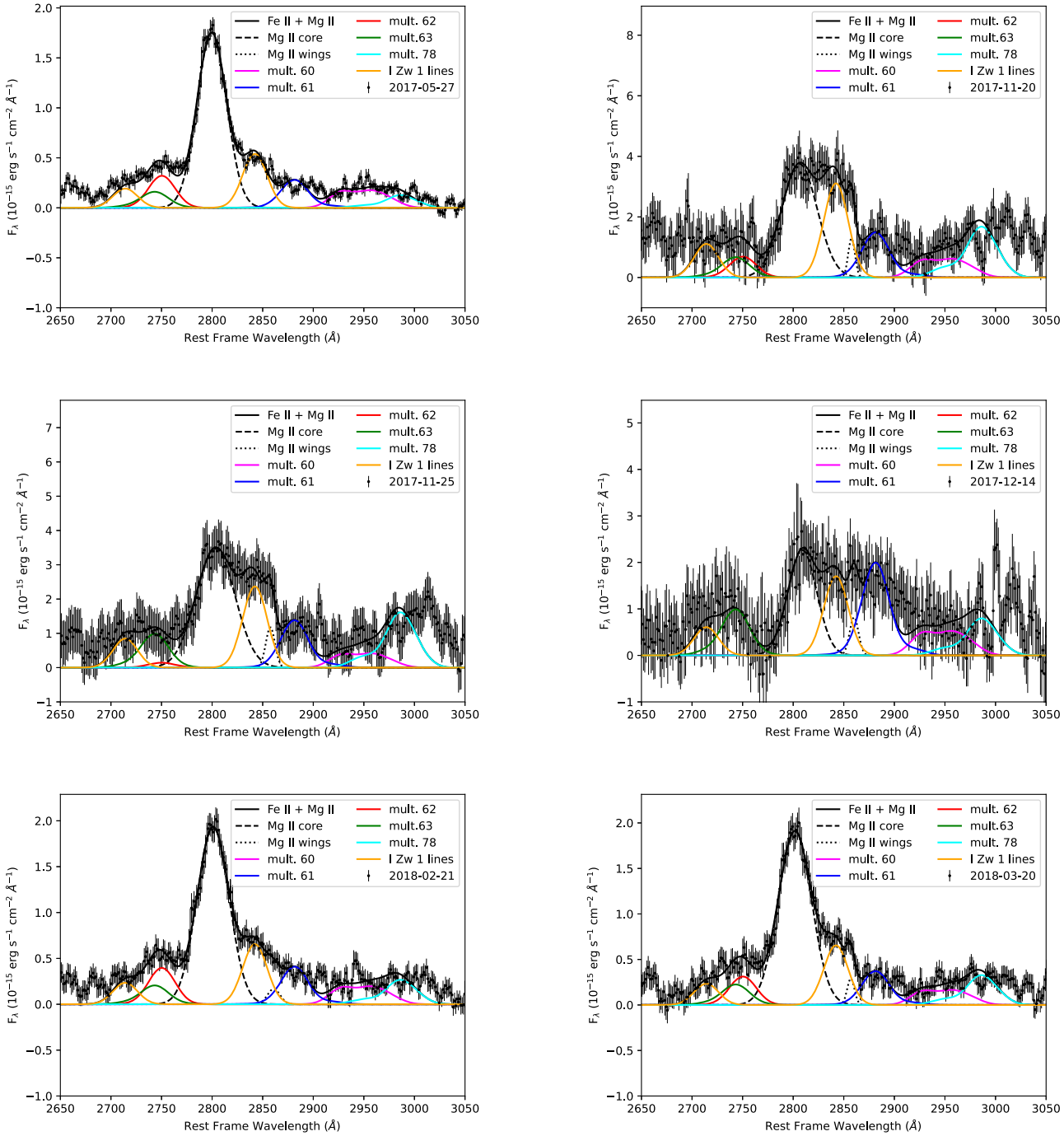

Figure 11. Fe II and continuum-subtracted spectra plotted with the best-fit Gaussian Mg II λ2798 emission-line profile and the scaled Fe II template from Popovic et al. (2018).

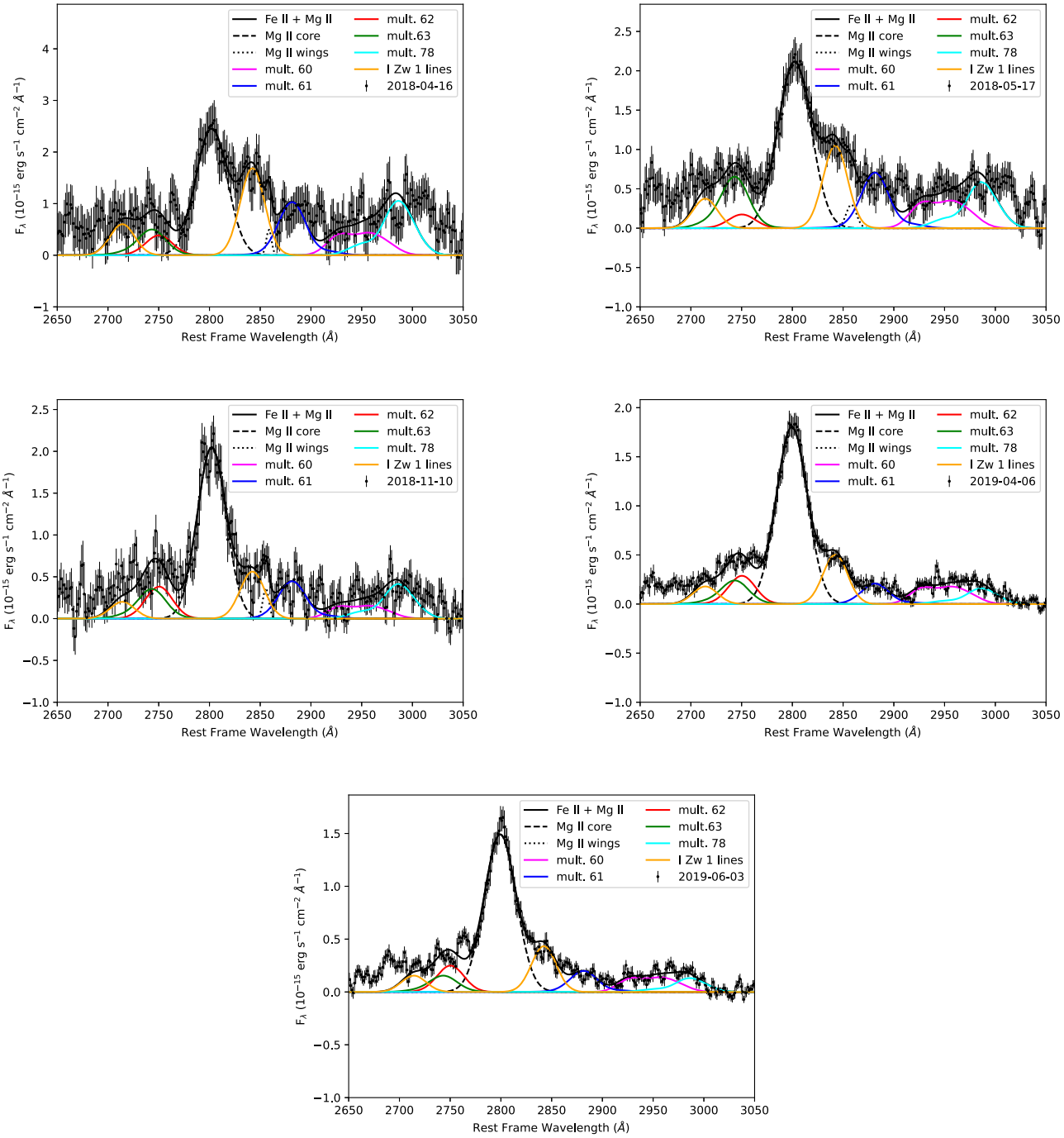

Figure 11. (Continued.)

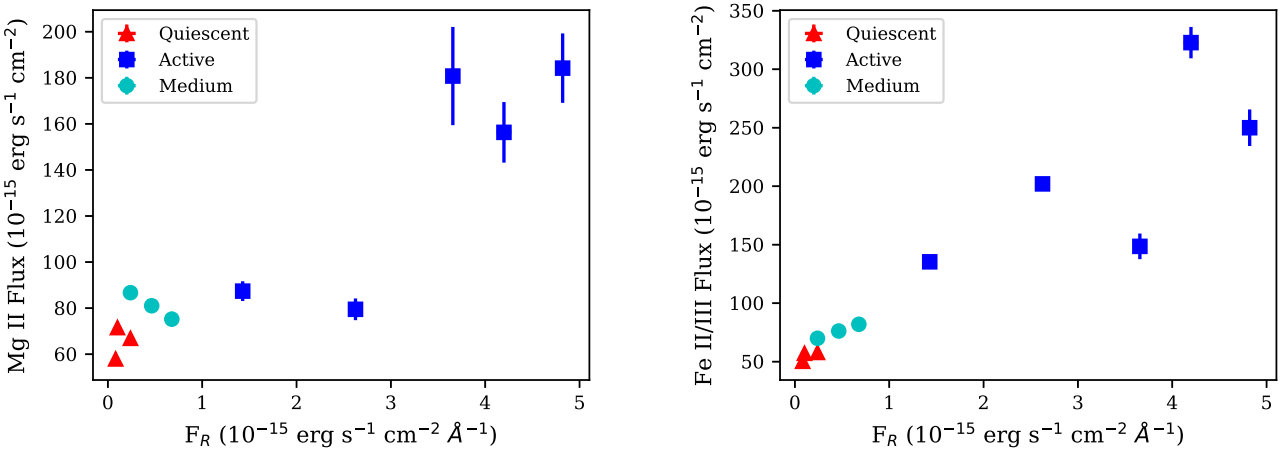

Figure 12. Emission-line fluxes of Mg II (left) and Fe II (right) when the Fe template from Popovic et al. (2018) was used versus the *R*-band flux density.

ORCID iDs

Melissa K. Hallum https://orcid.org/0000-0002-6634-9673
Svetlana G. Jorstad https://orcid.org/0000-0001-6158-1708
Valeri M. Larionov https://orcid.org/0000-0002-4640-4356
Alan P. Marscher https://orcid.org/0000-0001-7396-3332
Manasvita Joshi https://orcid.org/0000-0003-1134-7352
Zachary R. Weaver https://orcid.org/0000-0001-6314-0690
Karen E. Williamson https://orcid.org/0000-0003-1318-8535
Iván Agudo https://orcid.org/0000-0002-3777-6182
Carolina Casadio https://orcid.org/0000-0003-1117-2863
Antonio Fuentes https://orcid.org/0000-0002-8773-4933
Evgenia N. Kopatskaya https://orcid.org/0000-0001-9518-337X
Elena G. Larionova https://orcid.org/0000-0002-2471-6500
Daria A. Morozova https://orcid.org/0000-0002-9407-7804
Anna A. Nikiforova https://orcid.org/0000-0001-9858-4355
Sergey S. Savchenko https://orcid.org/0000-0003-4147-3851
Ivan S. Troitsky https://orcid.org/0000-0002-4218-0148
Yulia V. Troitskaya https://orcid.org/0000-0002-9907-9876
Andrey A. Vasilyev https://orcid.org/0000-0002-8293-0214

References

Abdollahi, S., Acero, F., Ackermann, M., et al. 2020, ApJS, 247, 33
Ackermann, M., Ajello, M., Allafort, A., et al. 2014, ApJ, 786, 157
Aleksić, J., Antonelli, L. A., Antoranz, P., et al. 2011, ApJL, 730, L8
Baldwin, J. A., Ferland, G. J., Korista, K. T., Hamann, F., & LaCluyze, A. 2004, ApJ, 615, 610
Bayer, M. 2012, in The Architecture of Open Source Applications Volume II: Structure, Scale, and a Few More Fearless Hacks, ed. A. Brown & G. Wilson (Morrisville, NC: Lulu)
Błażejowski, M., Sikora, M., Moderski, R., & Madejski, G. M. 2000, ApJ, 545, 107
Bloom, S. D., & Marscher, A. P. 1996, ApJ, 461, 657
Boroson, T. A., & Green, R. F. 1992, ApJS, 80, 109
Böttcher, M., Reimer, A., Sweeney, K., & Prakash, A. 2013, ApJ, 768, 54
Castelli, F., & Kurucz, R. 1994, A&A, 281, 218
Cielo, S., Antonuccio-Delogu, V., Macciò, A. V., Romeo, A. D., & Silk, J. 2014, MNRAS, 439, 2903
de la Peña, F., Prestat, E., Fauske, V. T., et al. 2021, hyperspy/hyperspy: Release v1.6.4, v1.6.4, Zenodo, doi:10.5281/zenodo.5082777
Dermer, C. D., & Schlickeiser, R. 1994, ApJS, 90, 945
Earl, N., Tollerud, E., Jones, C., et al. 2020, astropy/specutils: v1.5.0, Zenodo, doi:10.5281/zenodo.5721652
Elvis, M. 2017, ApJ, 847, 56
Fan, J., Tao, J., Qian, B., et al. 2006, PASJ, 58, 797
Ghisellini, G., Tavecchio, F., Maraschi, L., Celotti, A., & Sbarrato, T. 2014, Natur, 515, 376
Grandi, S. A. 1982, ApJ, 255, 25
Harris, C. R., Millman, K. J., van der Walt, S. J., et al. 2020, Natur, 585, 357
Hewett, P. C., & Wild, V. 2010, MNRAS, 405, 2302
Hovatta, T., Tornikoski, M., Lainela, M., et al. 2007, AJ, 133, 1947
Hunter, J. D. 2007, CSE, 9, 90
Isler, J. C., Urry, C. M., Bailyn, C., et al. 2015, ApJ, 804, 7
Jorstad, S., & Marscher, A. 2016, Galax, 4, 47
Jorstad, S., Marscher, A., Larionov, V., et al. 2010, ApJ, 715, 362
Jorstad, S., Marscher, A., Smith, P., et al. 2013, ApJ, 773, 147
Jorstad, S. G., Marscher, A. P., Morozova, D. A., et al. 2017, ApJ, 846, 98
Joshi, M., Marscher, A. P., & Böttcher, M. 2014, ApJ, 785, 132
Keck, M. 2019, PhD thesis, Boston Univ.
Kovačević, J., Popović, L. Č., & Kollatschny, W. 2014, AdSpR, 54, 1347
Larionov, V., Jorstad, S., Marscher, A., et al. 2017, Galax, 5, 91
Larionov, V., Jorstad, S., Marscher, A., et al. 2020, MNRAS, 492, 3829
Lebigot, E. O. 2020, Uncertainties: a Python package for calculations with uncertainties, https://pythonhosted.org/uncertainties/
León-Tavares, J., Chavushyan, V., Lobanov, A., Valtaoja, E., & Arshakian, T. G. 2015, in Extragalactic Jets from Every Angle, IAU Symp. 313 Vol. 313 (Cambridge: Cambridge Univ. Press), 43
León-Tavares, J., Chavushyan, V., Patiño Álvarez, V., et al. 2013, ApJL, 763, L36
Lister, M., Aller, M., Aller, H., et al. 2016, AJ, 152, 12
MacDonald, N. R., Marscher, A. P., Jorstad, S. G., & Joshi, M. 2015, ApJ, 804, 111
McHardy, I. M., Marscher, A. P., Gear, W. K., et al. 1990, MNRAS, 246, 305
Mead, A., Ballard, K., Brand, P., et al. 1990, A&AS, 83, 183
Mirzoyan, R. 2017, Atel, 11061, 1
Mukherjee, R. 2017, Atel, 11075, 1
Nalewajko, K., Begelman, M. C., & Sikora, M. 2014, ApJ, 789, 161
Newville, M., Stensitzki, T., Allen, D. B., & Ingargiola, A. 2014, Ingargiola, A. 2014, LMFIT: Non-Linear Least-Square Minimization and Curve-Fitting for Python, 0.8.0, Zenodo, doi:10.5281/zenodo.11813
Nolan, P. L., Abdo, A. A., Ackermann, M., et al. 2012, ApJS, 199, 31
Norman, C., & Miley, G. 1984, A&A, 141, 85
Perucho, M., Martí, J.-M., & Quilis, V. 2019, MNRAS, 482, 3718
Peterson, B. M., Wanders, I., Horne, K., et al. 1998, PASP, 110, 660
Popovic, L. C., Ilic, D., Bon, E., et al. 2018, POBeo, 98, 49
Punsly, B. 2013, ApJL, 762, L25
Raiteri, C., Villata, M., Lanteri, L., et al. 1998, A&AS, 130, 495
Ramakrishnan, V., León-Tavares, J., Rastorgueva-Foi, E. A., et al. 2014, MNRAS, 445, 1636
Reback, J., McKinney, W., Jbrockmendel, et al. 2020, pandas-dev/pandas: Pandas 1.1.4, Zenodo, doi:10.5281/zenodo.3509134
Sameshima, H., Kawara, K., Matsuoka, Y., et al. 2011, MNRAS, 410, 1018
Savolainen, T., & Kovalev, Y. 2008, A&A, 489, L33
Schmidt, G., Stockman, H., & Smith, P. 1992, ApJL, 398, L57
SciPy 1.0 Contributors, Virtanen, P., Gommers, R., et al. 2020, NatMe, 17, 261
Sikora, M., Begelman, M. C., & Rees, M. J. 1994, ApJ, 421, 153
Sikora, M., Stawarz, Ł., Moderski, R., Nalewajko, K., & Madejski, G. M. 2009, ApJ, 704, 38
Smith, P. 2016, Galax, 4, 27
Smith, P. S., Montiel, E., Rightley, S., et al. 2009, arXiv:0912.3621

Sokolov, A., & Marscher, A. P. 2005, ApJ, 629, 52
Stoehr, F., White, R., Smith, M., et al. 2008, in ASP Conf. Ser. 394, Astronomical Data Analysis Software and Systems XVII, ed. R. W. Argyle, P. S. Bunclark, & J. R. Lewis (Francisco, CA: ASP), 505
Sun, M., Grier, C. J., & Peterson, B. M. 2018, PyCCF: Python Cross Correlation Function for reverberation mapping studies, ascl:1805.032
The Astropy Collaboration, Price-Whelan, A. M., Sipőcz, B. M., et al. 2018, AJ, 156, 123
The Astropy Collaboration, Robitaille, T. P., Tollerud, E. J., et al. 2013, A&A, 558, A33
Thompson, D. J., Bertsch, D. L., Dingus, B. L., et al. 1995, ApJS, 101, 259
Tsuzuki, Y., Kawara, K., Yoshii, Y., et al. 2006, ApJ, 650, 57
Urry, C. M., & Padovani, P. 1995, PASP, 107, 803
Vacca, W. D., Cushing, M. C., & Rayner, J. T. 2003, PASP, 115, 389
Vestergaard, M., & Wilkes, B. J. 2001, ApJ, 134, 1
Wardle, J., & Kronberg, P. 1974, ApJ, 194, 249
Weaver, Z. R., Balonek, T. J., Jorstad, S. G., et al. 2019, ApJ, 875, 15
Williamson, K. E., Jorstad, S. G., Marscher, A. P., et al. 2014, ApJ, 789, 135
Wills, B., Pollock, J., Aller, H., et al. 1983, ApJ, 274, 62
Wills, B., Wills, D., Breger, M., et al. 1992, ApJ, 398, 454
Zhou, H., Shi, X., Yuan, W., et al. 2019, Natur, 573, 83